Inorganic Chemistry

Article

pubs.acs.org/IC

Molecular Design for Tailoring a Single-Source Precursor for Bismuth Ferrite

Georg Bendt,[†] Rafael Schiwon,[‡] Soma Salamon,[§] Joachim Landers,[§] Ulrich Hagemann,[∥] Christian Limberg,*[,‡] Heiko Wende,[§] and Stephan Schulz*[,†]

[†]Faculty of Chemistry, Inorganic Chemistry, and Center for Nanointegration Duisburg-Essen (CENIDE), University of Duisburg-Essen, Universitätsstrasse 7, 45114 Essen, Germany

[§]Faculty of Physics and Center for Nanointegration Duisburg-Essen (CENIDE), University of Duisburg-Essen, Lotharstrasse 1, 47048 Duisburg, Germany

[‡]Institut für Chemie, Humboldt-Universität zu Berlin, Brook-Taylor-Straße 2, 12489 Berlin, Germany

[∥]Interdisciplinary Center for Analytics on the Nanoscale, Nano Energie Technik Zentrum, Carl-Benz-Strasse 199, 47047 Duisburg, Germany

Supporting Information

ABSTRACT: Nearly phase-pure bismuth ferrite particles were formed by thermolysis of the *single-source precursor* $[Cp(CO)_2FeBi(OAc)_2]$ (**1**) in octadecene at 245 °C, followed by subsequent calcination at 600 °C for 3 h. In contrast, the slightly modified compound $[Cp(CO)_2FeBi(O_2C^tBu)_2]$ (**2**) yielded only mixtures of different bismuth oxide phases, revealing the distinctive influence of molecular design in material synthesis. The chemical composition, morphology, and crystallinity of the resulting materials were investigated by X-ray diffraction, transmission electron microscopy, and energy-dispersive X-ray spectroscopy. In addition, the optical properties were investigated by Fourier transform infrared and UV−vis spectroscopies, showing a strong band gap absorption in the visible range at 590 nm (2.2 eV). The magnetic behavior was probed by vibrating-sample and superconducting quantum interference device magnetometry, as well as ^{57}Fe Mössbauer spectroscopy.

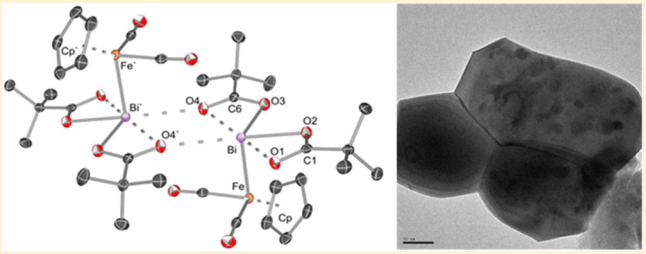

INTRODUCTION

The use of single-source precursors (SSPs) as starting compounds for the formation of nanoparticles and thin films is a promising alternative approach for the synthesis of high-quality materials.[1−3] SSPs already contain the elements of the desired material in a single molecule, and their thermal properties and decomposition pathways can be modified by the precursor design; in particular, the loss of highly volatile elements during synthesis resulting in off-stoichiometric products can be avoided. $BiFeO_3$ combines antiferromagnetic and ferroelectric behavior and belongs to the family of so-called multiferroics.[4] To the best of the authors' knowledge, $BiFeO_3$ is the only multiferroic material that retains its properties above room temperature with an antiferromagnetic Néel temperature TN = 370 °C and a ferroelectric Curie temperature T_C = 830 °C. $BiFeO_3$ crystallizes in the rhombohedrally distorted perovskite structure with lattice constants a = 5.58 Å and c = 13.87 Å in the hexagonal representation. The multiferroic nature can be explained by the displacement of Fe^{3+} and Bi^{3+} along the c axis and a canted ordering of the Fe^{3+} spins, leading to a cycloidal spin ordering with a period length of 62 nm.[5−7] Moreover, $BiFeO_3$ exhibits a band gap (2.1−2.8 eV) in the visible range, making it also an ideal candidate for photocatalytic applications, i.e. the degradation of organic molecules[8−10] and also water splitting.[11,12]

The synthesis of $BiFeO_3$ is afflicted with several problems; the ternary bismuth−iron−oxygen phase diagram shows multiple bismuth-rich phases including $Bi_2Fe_4O_9$ and $Bi_{25}FeO_{40}$, which are often seen as parasitic phases. Furthermore, a high leak current due to defects, mostly oxygen vacancies and impurities (Fe^{2+} ions), limits the technical application.[13,14] Several synthetic strategies have been developed for the formation of $BiFeO_3$, including solid-state,[15] sol−gel,[16] hydrothermal as well as microwave-assisted hydrothermal,[17] self-combustion,[18] and electrospinning[19] reactions. The most common precursors are bismuth and iron nitrates. However, while SSPs for the solution-based synthesis of $BiFeO_3$ are unknown, to date, Blackman et al. investigated the heterobimetallic compound $[Cp(CO)_2FeBiCl_2]$ (Cp = η^5-C_5H_5) as the aerosol-assisted chemical vapor deposition precursor for the deposition of $BiFeO_3$ onto different substrates at 300 °C with subsequent annealing at 500−700 °C.[20] The phase-pure films obtained at 700 °C exhibit a direct band gap at

Received: April 16, 2016

DOI: 10.1021/acs.inorgchem.6b00951
Inorg. Chem. XXXX, XXX, XXX−XXX

2.1 eV and high activity for water oxidation under visible-light irradiation.

Recently, we reported a precedent case, proving that molecular Fe−Bi entities can be constructed by the reactions of complexes with Fe−Fe bonds and bismuth carboxylates: The reaction between $[Cp(CO)_2Fe]_2$ and $[Bi(OAc)_3]$ yielded $[Cp(CO)_2FeBi(OAc)_2]$ (**1**; Figure 1).[21] Herein we describe our results in testing **1** as well as the newly prepared derivative $[Cp(CO)_2FeBi(O_2C^tBu)_2]$ (**2**), varying in the carboxylate residue, as SSPs.

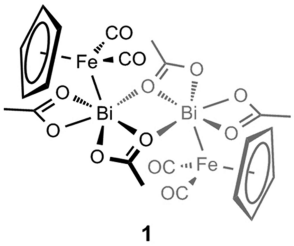

1

Figure 1. Molecular structure of iron−bismuth compound **1**.[22]

RESULTS AND DISCUSSION

After the successful preparation of **1**, we have been able to show that, setting out from $[Cp(CO)_2Fe]_2$ ($[Fp]_2$), also $[FpBi(O_2CH)_2]_n$ is accessible via a reaction with bismuth formate;[21b] because of aggregation to a coordination polymer, the product was, however, only sparingly soluble in common organic solvents. Aiming at soluble derivatives and further support that indeed reactions of $[Fp]_2$ with bismuth carboxylates provide more general access to molecular bismuth−iron compounds, we have thus treated $[Cp(CO)_2Fe]_2$ with bismuth pivalate instead of bismuth acetate. The stirring of an equimolar $[Fp]_2$/$[Bi(O_2C^tBu)_3]$ suspension in dichloromethane at room temperature for a period of 9 days resulted in a red solution, which was evaporated to dryness to yield a brown powder. Washing the residue with small portions of hexane and crystallization from a dichloromethane/hexane mixture led to red crystals of **2** in 53% yield. A single-crystal X-ray diffraction (XRD) analysis revealed that **2** crystallizes as a dimer (with a crystallographic inversion center) similar to that of the acetate **1** (Figure 2).

Each bismuth atom is bound to one organometallic iron fragment via a Fe−Bi metal bond [2.6072(4) Å], which is longer than the corresponding distance in **1** [Fe−Bi 2.585(2) Å]. Additionally, two covalent bonds to two pivalate ligands are formed [Bi−O2:2.2978(18) Å; Bi−O3:2.3277(18) Å] with distances that are also longer than the corresponding distances in **1** [d(Bi−O) = 2.342−2.353 Å]. The angle between these oxygen atoms [O2−Bi−O3 79.73(6) Å] and also all of the Fe−Bi−O angles [92.56(4)−95.23(5)°] indicate that these covalent bonds are mainly established through p orbitals at the bismuth atom. The corresponding carbonyl units of the carboxylate ligands also interact with the respective bismuth centers, and one of them per molecule is further involved in a secondary Bi···O−Bi′ contact with the bismuth atom of a second molecule [O4′···Bi and O4···Bi′ 2.7971(18) Å]. As the second molecule bonds back via an analogous interaction, a dimer is thus created featuring a $[Bi_2O_2]$ diamond core motif with larger Bi−O′ and Bi···Bi′ distances [4.4989(4) Å] compared to those in **1** [d(Bi−O′) = 2.711(4) Å; d(Bi−Bi′) = 4.3485(6) Å].

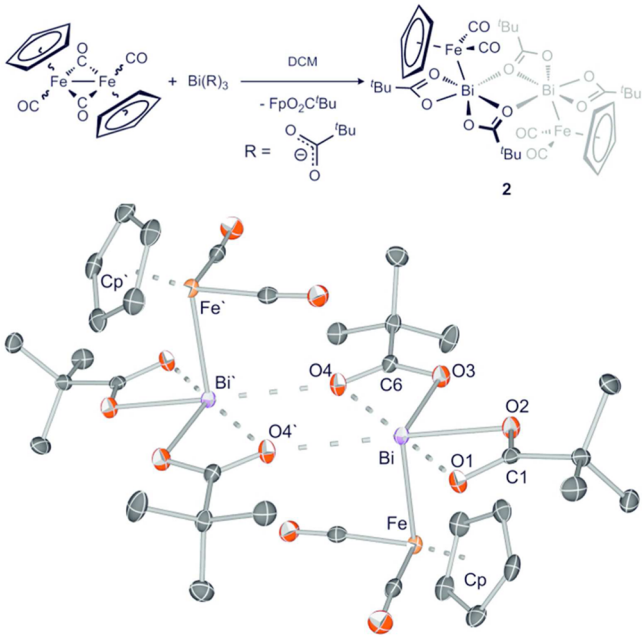

Figure 2. Synthesis of **2** by the reaction of $[Fp]_2$ with $[Bi(O_2C^tBu)_3]$ and molecular structure of **2**. Displacement ellipsoids are shown at the 50% probability level. Hydrogen atoms are omitted for clarity. Selected bond lengths (Å) and angles (deg): Fe−Bi 2.6072(4), Bi−O2 2.2978(18), Bi−O3 2.3277(18), Bi···O1 2.6298(17), Bi···O4 2.6312(17), Bi···O4′ 2.7971(18), C1−O1 1.249(3), C1−O2 1.285(3), C6−O4 1.251(3), C6−O3 1.286(3), Bi···Bi′ 4.4989(4); Cp−Fe−Bi 122.919(16), O2−Bi−O3 79.73(6), O2−Bi−Fe 95.09(5), O3−Bi−Fe 95.23(5), O2−Bi···O4′ 157.455(60), O1···Bi···O4 171.07(6).

Figure 3 displays the results obtained from thermogravimetric analysis (TGA) investigations (see also Figures S1 and S2), showing that compounds **1** and **2** cannot be transferred into the gas phase under normal pressure without decomposition, so that determination of their potential as SSPs for chemical vapor deposition requires more studies under authentic conditions. We have therefore examined their behavior as SSPs in solution, as described below.

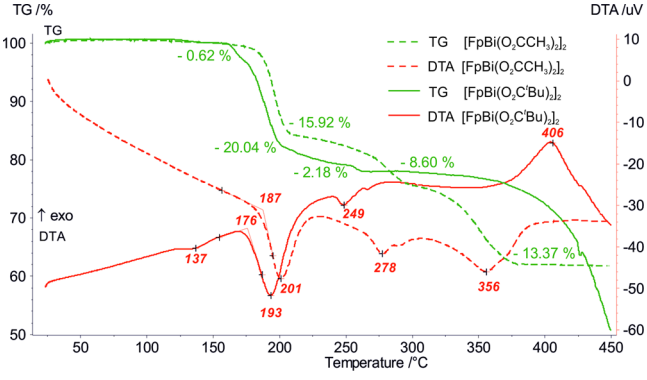

Figure 3. Simultaneous thermal analysis measurement (argon purge gas, 60 mL/min, heating rate 10 K/min) of **1** (dashed lines) and **2** (solid lines). TGA is shown in green, and differential thermal analysis (DTA) is shown in red.

Thermolysis reactions were performed first with 200 mg of **1**, which was suspended in 10 mL of octadecene, slowly heated to 215, 230, and 245 °C in order to investigate the role of the

DOI: 10.1021/acs.inorgchem.6b00951
Inorg. Chem. XXXX, XXX, XXX−XXX

reaction temperature, and stirred for 1 h. The orange suspension turned to a black suspension around 200 °C. After cooling to ambient temperature, the decomposition products were isolated by centrifugation and repeatedly washed with chloroform. The chemical composition of the resulting materials was analyzed by energy-dispersive X-ray spectroscopy (EDX). The product obtained at 245 °C shows a composition of 20 atom % bismuth, 20 atom % iron, and 60 atom % oxygen, corresponding to a bismuth-to-iron atomic ratio of close to 1, indicating complete decomposition of the precursor, while the products obtained at lower temperatures are bismuth-rich. In addition, the EDX analyses of all three samples reveal high carbon contents, which are not taken into account, indicating the presence of organic groups.

The samples were further investigated by IR spectroscopy. In Figure 4, the Fourier transform infrared (FTIR) spectra of

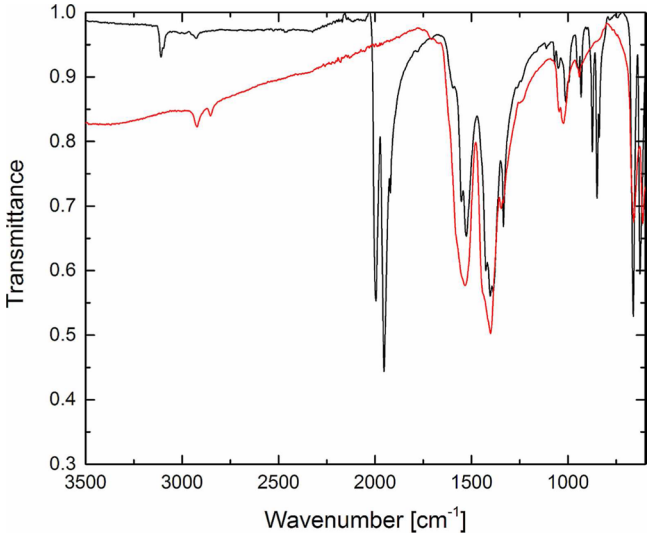

Figure 4. FTIR spectra of precursor **1** (black) and the decomposition product obtained at 245 °C after workup (red).

precursor **1** (black) and the as-obtained decomposition product at 245 °C (red) are displayed. Compared to the precursor, the black powder shows the loss of characteristic absorption bands around 2000 cm^{-1} for the carbonyl ligands, whereas the bands for the carboxylate group around 1500 cm^{-1} are still present.

In order to obtain crystalline $BiFeO_3$, the amorphous black powders were annealed at 600 °C for 3 h in air. The resulting products showed the characteristic orange color of $BiFeO_3$.

The XRD patterns of the annealed powders are displayed in Figure 5. The powders obtained at 215 and 230 °C after annealing consist of different phases with $BiFeO_3$ (PDF 71-2494) as the major phase and $Bi_2Fe_4O_9$ (PDF 71-2494) and $Bi_{25}FeO_{40}$ (PDF 71-2494) as minor phases. The results of quantitative phase analysis are displayed in Table 1. In contrast, the pattern of the annealed powder obtained at 245 °C can be indexed on the basis of a rhombohedrally distorted perovskite structure, which indicates the formation of nearly phase-pure $BiFeO_3$. The origin of the formation of bismuth-rich phases can be found in the high bismuth content of the decomposition product. The bismuth content is lower than that in the as-decomposed products, indicating the loss of bismuth or Bi_2O_3 due to their high vapor pressure.

The FTIR spectrum of the phase-pure $BiFeO_3$ (sample III, Figure 6a) shows strong absorption bands around 530 and 430

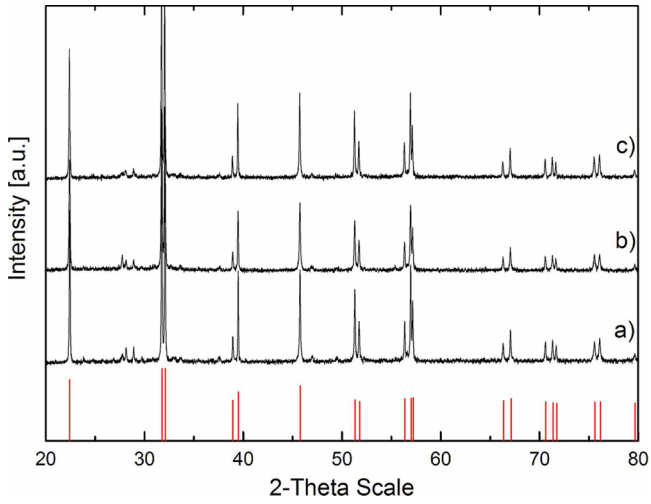

Figure 5. Powder XRD patterns of $BiFeO_3$ particles obtained by calcination of the decomposition product from precursor **1** at different temperatures (red: $BiFeO_3$, PDF 71-2494) in octadecene: (a) 215 °C; (b) 230 °C; (c) 245 °C.

Table 1. Bismuth-to-Iron Ratios for Different Samples As Determined by EDX Measurements and the Results of the Quantitative Rietveld Refinement for the Samples

sample	precursor	T_{decomp}	bismuth-to-iron ratio[a]	bismuth-to-iron ratio[b]	phase[c]
I	**1**	215	62:38	58:42	93.5 wt % $BiFeO_3$
					6.5 wt % $Bi_2Fe_4O_9$
II	**1**	230	57:43	54:46	87.7 wt % $BiFeO_3$
					8.6 wt % $Bi_2Fe_4O_9$
					3.4 wt % $Bi_{25}FeO_{39}$
III	**1**	245	53:47	51:49	82.0 wt % $BiFeO_3$
					12.6 wt % $Bi_2Fe_4O_9$
					5.4 wt % $Bi_{25}FeO_{39}$
IV	**2**	215	100:0	100:0	Bi_2O_3
V	**2**	245	100:0	100:0	Bi_2O_3

[a]EDX before calcination. [b]EDX after calcination. [c]As determined by XRD.

cm^{-1} related to the characteristic stretching and bending of the Fe−O bonds in the FeO_6 octahedron, the main building block of the perovskite structure. In order to determine the band gap of the $BiFeO_3$ powder, UV−vis diffuse-reflectance spectra were recorded. Applying the Kubelka−Munk function leads to a band gap energy of 2.2 eV (Figure 6b).

Figure 7 displays a typical transmission electron microscopy (TEM) image obtained from the phase-pure $BiFeO_3$ crystallites, showing a relatively broad size distribution between 100 and 200 nm. The crystalline particles, which are electron transparent, as can be seen in Figure 7c, are sintered together by thermal treatment (annealing). High-resolution TEM and selected-area electron diffraction (SAED) of a single particle demonstrate their highly crystalline nature, as was expected from the powder XRD studies.

DOI: 10.1021/acs.inorgchem.6b00951
Inorg. Chem. XXXX, XXX, XXX−XXX

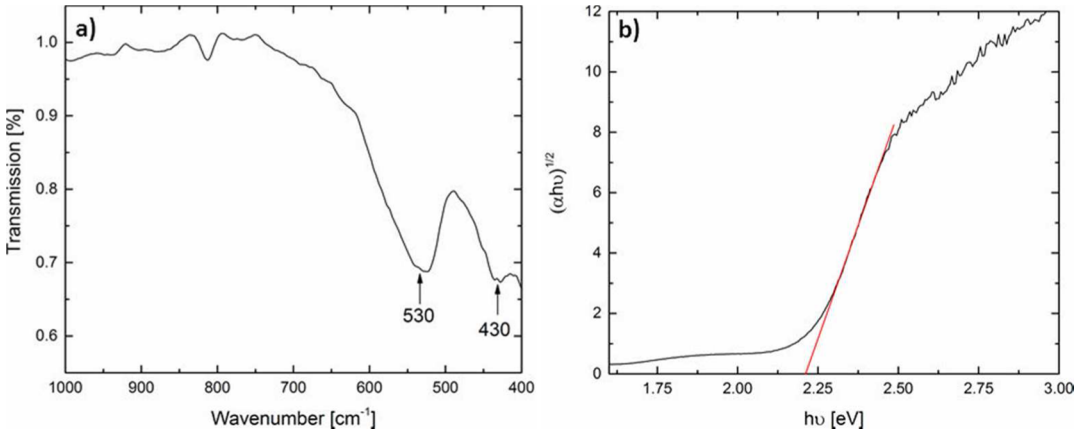

Figure 6. Typical FTIR spectrum of $BiFeO_3$ powder (sample III, a) and Tauc plot for determining the optical band gap (b).

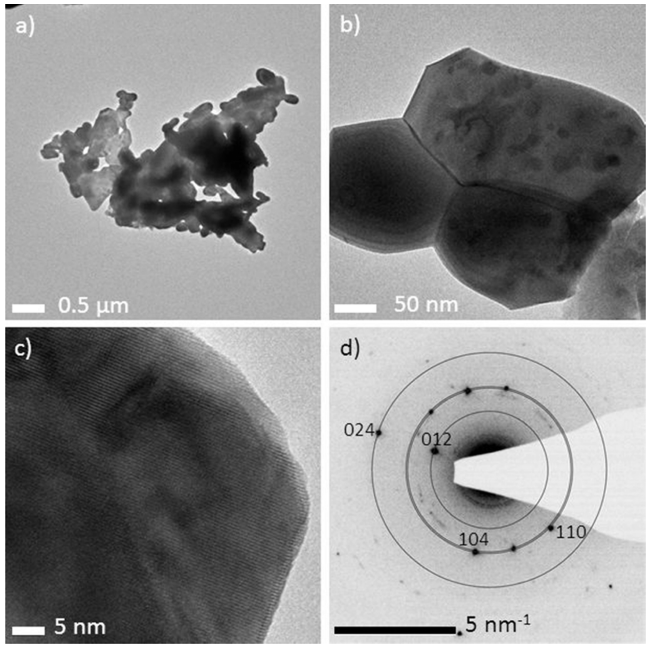

Figure 7. TEM images (a–c) and SAED pattern (d) of sample **III**. Scale bars: 0.5 μm (a); 50 nm (b); 5 nm (c); 5 nm (d).

X-ray photoelectron spectroscopy (XPS) is very sensitive to the oxidation state of metals. The XPS measurement of sample III confirms the presence of bismuth, iron, and oxygen. In addition a small amount of carbon is detected. Soft Ion sputtering ,using 500V Ar^+ ions, shows that the carbon is not only due to surface contamination but also originiates from the material itself, indicating an incomplete decomposition of the precursor. The high-resolution spectrum of the Bi 4f peaks shows the characteristic peaks at 164 and 159 eV corresponding to Bi^{3+}. For iron, the Fe 2p peaks at 724 and 710 eV, and especially the existence and position of the Fe 2p satellite at 719 eV, indicate only the presence of Fe^{3+} cations; no peaks corresponding to Fe^{2+} are found (Figure 8).

In order to investigate the influence of the precursor design on the decomposition pathway, **2** was also investigated as a potential precursor for $BiFeO_3$, and the results were compared to those obtained with precursor **1**, which contains acetate instead of pivalate groups. The thermolysis reaction was performed with 200 mg of **2** suspended in 10 mL of octadecene, slowly heated to 215 and 245 °C, and stirred for 1 h. The red suspension turned black around 200 °C. After cooling to ambient temperature, the decomposition products were isolated by centrifugation and repeatedly washed with chloroform.

The chemical composition of the resulting materials was analyzed by EDX (Table 1). Both products, obtained at 215 and 245 °C, showed only the presence of bismuth and carbon. The IR spectrum of the washed powder shows weak absorption bands, indicating the presence of traces of intact precursor molecules (Figure 9). After thermal treatment at 600 °C for 3 h, yellow powders were obtained. As expected from the EDX results of the black powder, the XRD pattern showed the presence of Bi_2O_3 (PDF 41-1449) as the major product and traces of the nonstoichiometric phase $Bi_2O_{2.33}$ (PDF 27-0051; Figure 10).

The magnetic properties of sample **III** were investigated by vibrating-sample (VSM) and superconducting quantum interference device (SQUID) magnetometry. The 300 K $M(H)$ magnetization curve displayed in Figure 11 shows a linear response in the high-field range, often seen in antiferromagnetic samples. In the low-field range, a weak ferromagnetic signal due to canted antiferromagnetically coupled spins is visible. The maximum magnetization at room temperature was determined to be 0.73 emu/g at 9 T, which is large compared to that of bulk $BiFeO_3$, presumably because of uncompensated surface spins and size effects.[23] The 5 K magnetization curve shows an open hysteresis that was not visible in the 300 K curve, indicating superparamagnetic behavior also visible in the temperature-dependent magnetization: The $M(T)$ data shown in Figure 11 reveal a clear splitting between field-cooled (FC) and zero-field-cooled (ZFC) magnetization at low temperatures, corresponding to Néel relaxation behavior of the smaller particles within the sample, in agreement with the beginning superparamagnetic doublet visible in the room temperature Mössbauer spectrum. Furthermore, a clear cusp is visible in both the ZFC and FC curves at a temperature of 236 ± 3 K, marked by arrows. This indicates the presence of a minor $Bi_2Fe_4O_9$ phase; this material is reported to show an antiferromagnetic-to-paramagnetic transition in the range of about 250–260 K,[24,25] presumably decreased here by size effects. Because of its antiferromagnetic behavior, it has no noticeable influence on the $M(H)$ curves shown earlier. The presence of a small amount of $Bi_2Fe_4O_9$ is also verified by Mössbauer spectroscopy, as described in detail below.

Mössbauer spectra were recorded at room temperature (300 K), 80 K, and 4.3 K, and hyperfine parameters of the spectrum

DOI: 10.1021/acs.inorgchem.6b00951
Inorg. Chem. XXXX, XXX, XXX–XXX

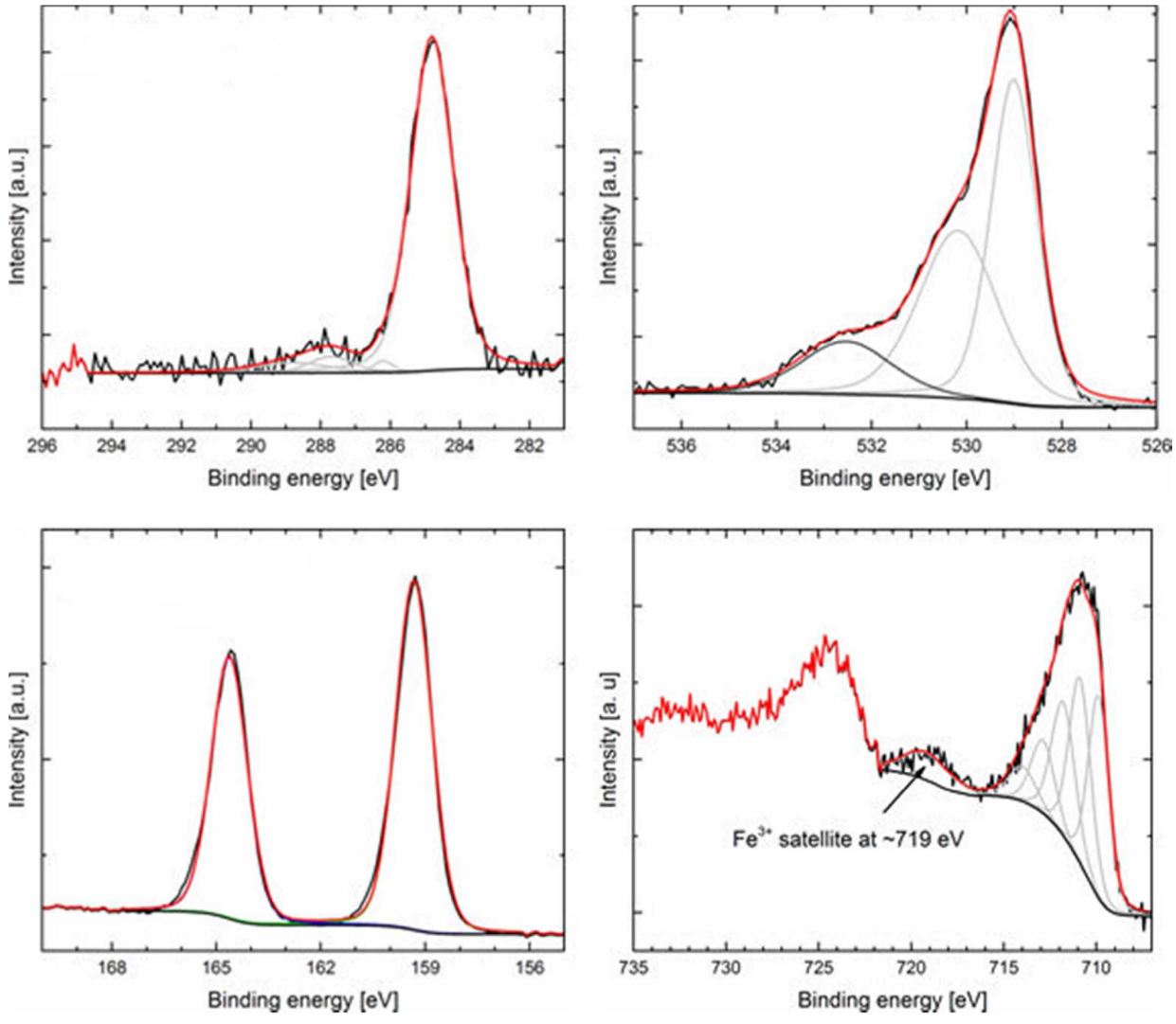

Figure 8. C 1s, O 1s, Fe 2p, and Bi 4f XPS spectra of $BiFeO_3$ (sample III): experimental data (black), envelope (red), and deconvoluted (gray) peaks.

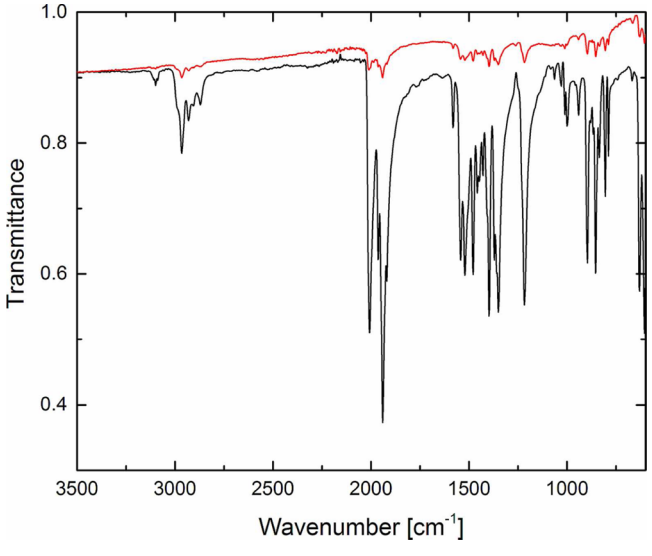

Figure 9. FTIR spectra of precursor **2** (black) and the decomposition product obtained at 245 °C after workup (red).

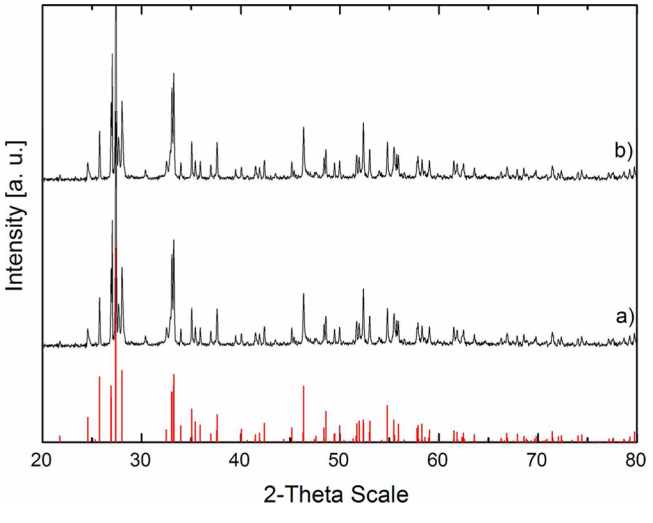

Figure 10. Powder XRD patterns of Bi_2O_3 particles after calcination of the decomposition product from precursor **2** at different temperatures (red: Bi_2O_3, PDF 41-1449): (a) 215 °C; (b) 245 °C.

DOI: 10.1021/acs.inorgchem.6b00951
Inorg. Chem. XXXX, XXX, XXX−XXX

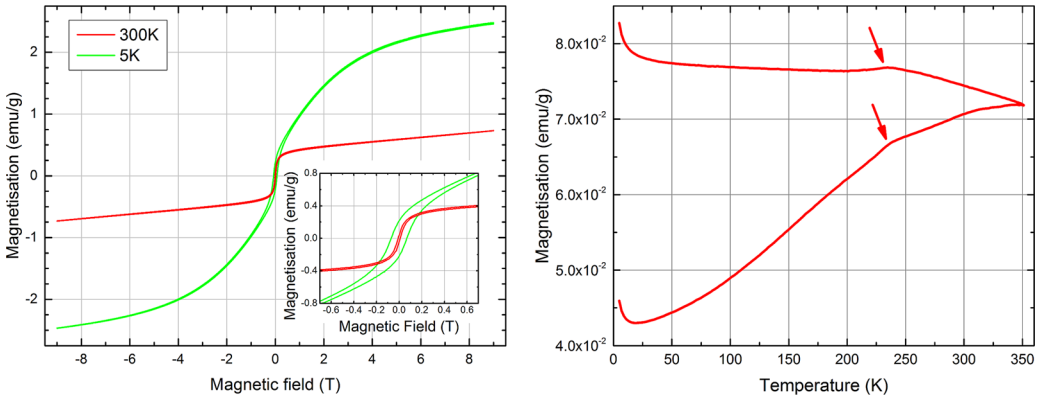

Figure 11. $M(H)$ loops of sample **III** at 300 and 5 K (left). The inset shows a magnification of the low-field regime. ZFC−FC $M(T)$ measurement performed at 10 mT (right).

at 80 K are shown representatively in Table 2, displaying good agreement with data previously reported for $BiFeO_3$ (full details are given in Table S1).[23,26,27] As is visible in Figure 12a, the room temperature spectrum is composed of a sextet corresponding to an antiferromagnetically coupled $BiFeO_3$ phase and several (super)paramagnetic doublets. The sextet displays a clearly visible asymmetry between opposite lines such as 1 and 6, which are often explained by an anisotropic hyperfine magnetic field, caused by the complex spin structure.[28] The latter leads to a distribution of hyperfine magnetic fields, which prevents the successful fitting of the spectrum using a single sextet. Therefore, a distribution of hyperfine magnetic fields with 40 equidistant subspectra was used to achieve a precise congruence between the measurement data and fit function. Because of the high Néel temperature of $BiFeO_3$, it is reasonable to assume that the dominant doublet is mainly caused by the superparamagnetic behavior of the smallest $BiFeO_3$ particles contained in the sample.[26,29] This is supported by spectra at 4.3 (Figure 12c) and 80 K (Figure 12b), which reveal a decrease in the doublet spectral area from ca. 13% at room temperature down to 5% at 80 K. However, the isomer shift shows a strong decrease from 300 to 80 K and little change from 80 to 4.3 K (see Table S1). We therefore assume that the small residual contribution at low temperatures is caused by a minute paramagnetic iron-bearing phase. The change in the isomer shift means that the majority of the doublet at 300 K is caused by superparamagnetic $BiFeO_3$, which becomes magnetically blocked at 80 K. When closely examining the low velocity range at the center of the room temperature spectrum, one can identify two additional doublets not belonging to the main $BiFeO_3$ doublet, matching hyperfine parameters of $Bi_2Fe_4O_9$ at room temperature.[30] This is further supported by the observation of two minor sextets of equal spectral area and with lower hyperfine magnetic fields compared to $BiFeO_3$ at 80 and 4.3 K, with hyperfine parameters, listed in Table 2 and SI, matching those of $Bi_2Fe_4O_9$.[31−33] Because $Bi_2Fe_4O_9$ has a higher iron content than $BiFeO_3$, the combined relative spectral area (proportional to the number of iron atoms) of ca. 9% corresponds to only 5−6 wt %.

Table 2. Hyperfine Parameters of Sample III at 80 K: Hyperfine Magnetic Field B_{hf}, Isomer Shift δ Relative to α-Iron at Room Temperature, Nuclear Quadrupole Level Shift 2ε, Respectively, Quadrupole Splitting ΔE_Q, and Relative Spectral Area A

	B_{hf} (T)	δ (mm/s)	$2\varepsilon/\Delta E_Q$ (mm/s)	A (%)
$BiFeO_3$	54.07 ± 0.03	0.50 ± 0.01	0.14 ± 0.01	86.0 ± 0.6
$BiFeO_3$ sp.		0.18 ± 0.01	0.45 ± 0.01	5.2 ± 0.1
$Bi_2Fe_4O_9$ I	44.15 ± 0.05	0.32 ± 0.01	0.12 ± 0.01	4.7 ± 0.1
$Bi_2Fe_4O_9$ II	47.65 ± 0.05	0.44 ± 0.01	0.31 ± 0.02	4.7 ± 0.2

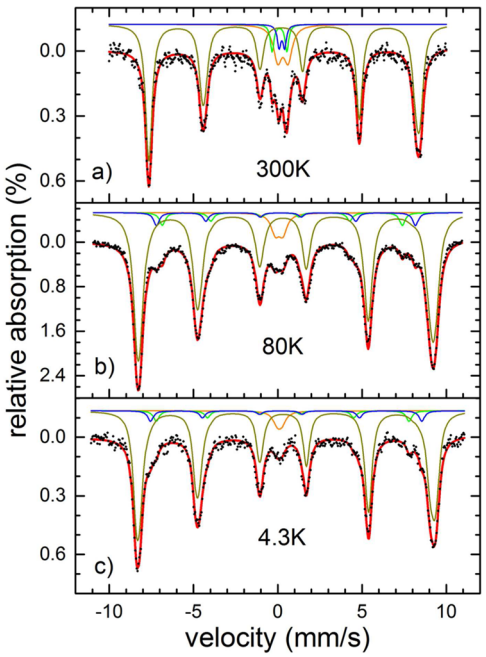

Figure 12. Mössbauer spectra recorded at 300 K (a), 80 K (b), and 4.3 K (c): experimental data (black symbols), sites I (tetrahedral) and II (octahedral) of $Bi_2Fe_4O_9$ (green and blue), magnetically coupled $BiFeO_3$ (brown), and superparamagnetic $BiFeO_3$ (orange), with the red line showing the overall theoretical spectrum.

CONCLUSIONS

First we report further precedence demonstrating that heterobimetallic iron−bismuth compounds can be obtained readily through reactions between $[Fp]_2$ and bismuth carboxylates. We have then provided evidence that such complexes can indeed serve as SSPs for the preparation of $BiFeO_3$ in the course of procedures involving thermal

DOI: 10.1021/acs.inorgchem.6b00951
Inorg. Chem. XXXX, XXX, XXX−XXX

treatment. Notably, our results also show that subtle changes within the precursor molecules have pronounced effects on the $BiFeO_3$ materials obtained; that is, the properties of the material generated are sensitively determined by the SSP, which motivates further efforts with respect to the modification of such systems.

Magnetometry indicates partial superparamagnetic behavior and the presence of a minor $Bi_2Fe_4O_9$ phase, while the saturation magnetization is slightly higher than that of bulk $BiFeO_3$, presumably due to size/surface effects. These findings support the results from Mössbauer spectroscopy and allow us to quantify the amount of $Bi_2Fe_4O_9$ to 5−6 wt %, while the $BiFeO_3$ parameters are in agreement with literature values. The determined amount of $Bi_2Fe_4O_9$ is in good agreement with the result of the quantitative Rietveld refinement.

EXPERIMENTAL SECTION

Synthetic Procedures, Materials, and Methods. Octadecene (Sigma-Aldrich) was carefully dried over a sodium/potassium alloy and degassed prior to use. $[Cp(CO)_2FeBi(OAc)_2]$ (**1**)[2] and $[Bi(O_2C^tBu)_3]$[3] were synthesized according to literature methods, while $[Fp]_2$ (99%, Acros Organics) was used as received. All synthetic steps were performed under an argon atmosphere using standard Schlenk techniques.

*η^5-Cyclopentadienyldicarbonyliron−bismuth Di-η^2-pivalate (**2**).* Solid $[Bi(O_2C^tBu)_3]$ (289.60 mg, 0.566 mmol, 1 equiv) was added to a suspension of $[Fp]_2$ (200 mg, 0.566 mmol, 1 equiv) in dichloromethane (10 mL) to give a red solution within 9 days at ambient temperature. Removing all volatiles at reduced pressure and washing the brown residue with three portions of 2 mL of hexane led to an orange powder, which was extracted with 9 mL of dichloromethane in small portions. The concentration of the combined extracts to 3 mL and layering of the solution with 9 mL of hexane resulted in the formation of red crystals of **2** within 7 days upon storing at −30 °C (yield: 177 mg, 0.301 mmol, 53%). ^{1}H NMR (C_6D_6, 300.13 MHz, 25 °C): δ 4.15 (s, 5 H, C_5H_5), 1.33 (s, 18 H, $C(CH_3)_3$). $^{13}C\{^1H\}$ NMR (C_6D_6, 75.47 MHz): δ 196.9 (2 C, *C*O), 187.5 (2 C, O(O)*C*C(CH$_3$)$_3$), 83.6 (5 C, C_5H_5), 41.1 (2 C, O(O)C*C*(CH$_3$)$_3$), 28.0 (2 C, *C*H$_3$). IR (KBr; cm^{-1}): ν 3926 s, 3107 s, 3098 s, 3089 s, 2965 m, 2931 s, 2906 s, 2870 s, 2015 sst, 1987 m, 1964 st, 1942 sst, 1920 m, 1582 s, 1547 m, 1525 m, 1507 s, 1480 m, 1460 s, 1448 s, 1430 s, 1398 m, 1370 m, 1350 m, 1351 m, 1219 m, 1088 s, 1066 s, 1030 s, 1013 s, 1001 s, 940 s, 901 s, 896 m, 876 s, 855 m, 839 s, 835 s, 804 m, 789 s, 634 m, 606 m, 579 m, 572 m, 537 s. 505 s, 454 s. Anal. Calcd for $C_{17}H_{23}BiFeO_6$ (588.19): C, 34.71; H, 3.94. Found: C, 35.02; H, 3.90.

Single-Crystal XRD. The data collection for **2** was performed with a Bruker D8 VENTURE area detector using Mo Kα radiation (λ = 0.71073 Å), and its crystallographic data are summerized in Table S1. Multiscan absorption corrections implemented in *SADABS*[34] were applied to the data. The structures were solved by intrinsic phasing (*SHELXS-97*)[35] and refined by full-matrix least-squares procedures on F^2 with all measured reflections (*SHELXL-2014*)[36] with anisotropic temperature factors for all non-hydrogen atoms. All hydrogen atoms were added geometrically and refined by using a riding model.

*Thermolysis of **1** and **2**.* A total of 200 mg (0.3 mmol) of the precursor was suspended in 10 mL of octadecene, and the suspension was heated to 215 °C (**1** and **2**), 230 °C (**1** and **2**), and 245 °C (**1**) for 1 h. After cooling to ambient temperature, the black precipitate was isolated by centrifugation and purified by repeated washing with *n*-hexane (two or three times). The dried solid was loaded in a ceramic boat and heated in a tube furnace to 600 °C with a heating rate of 10 K/min for 3 h.

Characterization. *Thermal Analysis.* A NETZSCH thermoanalyzer STA 409 C *Skimmer* system, equipped with a BALZERS QMG 421 spectrometer, was used to record the thermoanalytical curves. Further experimental details were as follows: DTA−TGA sample carrier system; Pt/PtRh10 thermocouples; platinum crucibles (beaker, 0.8 mL); sample mass 20−30 mg (measured versus empty reference crucible); constant purge gas flow of 100 mL/min argon 5.0 (AIRLIQUIDE); constant heating rate 10 K/min; raw data evaluation with manufacturer's software *PROTEUS* (version 4.3) without further data treatment, e.g., such as smoothing.

Powder XRD. XRD patterns were obtained at ambient temperature (25 ± 2 °C) using a Bruker D8 Advance powder diffractometer in Bragg−Brentano mode with Cu Kα radiation (λ = 1.5418 Å, 40 kV, and 40 mA). The powder samples were investigated in the range of 2θ = 5−90° with a step size of 2θ = 0.01° and a counting time of 0.3 s. Rietveld refinement was performed with the program package *TOPAS 4.2* from Bruker.

EDX Analysis. EDX studies were performed with a Jeol JSM 6510 scanning electron microscope equipped with an EDX device (Bruker Quantax 400).

TEM Analysis. TEM and SAED measurements were carried out on a Philips CM200 LaB_6 microscope operated at 200 kV. Samples for TEM observations were prepared by depositing a drop of a suspension of the material in ethanol onto a carbon-coated copper grid.

Magnetometry. Temperature-dependent magnetic measurements between 5 and 350 K were performed using a Quantum Design MPMS-5S, while the field-dependent $M(H)$ loops up to 9 T were recorded by a Quantum Design PPMS DynaCool using powder samples.

Mössbauer Spectroscopy. Mössbauer spectra were recorded in transmission geometry using a constant-acceleration spectrometer with a ^{57}Co source embedded in a rhodium matrix. $BiFeO_3$ powder was mixed with chemically inert boron nitride to obtain a sample with ca. 20 mg/cm^2 $BiFeO_3$. Measurements below room temperature were performed in a liquid-helium bath cryostat, while all spectrometers were calibrated using α-iron foil at room temperature. The experimental spectra were least-squares-fitted using the software package *"Pi"* by Ulrich von Hörsten.[37]

CCDC 1446539 (**2**) contains the supplementary crystallographic data for this paper. These data can also be obtained free of charge from The Cambridge Crystallographic Data Centre via www.ccdc.cam.ac.uk/data_request/cif.

ASSOCIATED CONTENT

Supporting Information

The Supporting Information is available free of charge on the ACS Publications website at DOI: 10.1021/acs.inorgchem.6b00951.

Simultaneous thermal analysis measurement of **1** and **2** and Mössbauer parameters for 300, 80, and 4.3 K for $BiFeO_3$, superparamagnetic $BiFeO_3$, and the tetrahedral (I) and octahedral (II) iron sites in $Bi_2Fe_4O_9$ (PDF)

CCDC 1446539 (**2**) (CIF)

AUTHOR INFORMATION

Corresponding Authors

*E-mail: christian.limberg@chemie.hu-berlin.de.

*E-mail: stephan.schulz@uni-due.de.

Author Contributions

The manuscript was written through contributions of all authors. All authors have given approval to the final version of the manuscript.

Notes

The authors declare no competing financial interest.

ACKNOWLEDGMENTS

This work was supported by the DFG (Grants SPP1681, WE2623/7-1, and WE2623/13-2) and by Stiftung Mercator (MERCUR). Financial support by the University of Duisburg-Essen is acknowledged by S.S. and H.W., while C.L. is grateful to the Humboldt-Universität zu Berlin for core support. We

DOI: 10.1021/acs.inorgchem.6b00951
Inorg. Chem. XXXX, XXX, XXX−XXX

thank Prof. Barcikowski, University of Duisburg-Essen, for the UV−vis spectrum, Prof. Pinna, Humboldt-Universität zu Berlin, for the TEM image, Nicolas Frank, Humboldt-Universität zu Berlin, for the single-crystal XRD study, and Dr. Michael Feist for TGA.

REFERENCES

(1) (a) Martin, L. W.; Chu, Y.-H.; Ramesh, R. *Mater. Sci. Eng., R* **2010**, *68*, 89−133. (b) Singh, M. K.; Yang, Y.; Takoudis, C. G. *Coord. Chem. Rev.* **2009**, *253*, 2920−2934. (c) Zhang, Q.; Sando, D.; Nagarajan, V. *J. Mater. Chem. C* **2016**, *4*, 4092−4124.
(2) (a) Bendt, G.; Weber, A.; Heimann, S.; Assenmacher, W.; Prymak, O.; Schulz, S. *Dalton Trans.* **2015**, *44*, 14272−14280. (b) Bendt, G.; Schulz, S.; Zastrow, S.; Nielsch, K. *Chem. Vap. Deposition* **2013**, *19*, 235−241. (c) Schulz, S.; Heimann, S.; Friedrich, J.; Engenhorst, M.; Schierning, G.; Assenmacher, W. *Chem. Mater.* **2012**, *24*, 2228−2234.
(3) (a) Lieberman, C. M.; Wei, Z.; Filatov, A. S.; Dikarev, E. V. *Inorg. Chem.* **2016**, *55*, 3946−3951. (b) Moniz, S. J. A.; Pugh, D.; Blackman, C. S.; Tang, J.; Carmalt, C. *Cryst. Growth Des.* **2016**, DOI: 10.1021/acs.cgd.6b00370.
(4) Catalan, G.; Scott, J. F. *Adv. Mater.* **2009**, *21*, 2463−2485.
(5) Fischer, P.; Polomska, M.; Sosnowska, I.; Szymanski, M. *J. Phys. C: Solid State Phys.* **1980**, *13*, 1931−1940.
(6) Sosnowska, I.; Peterlin-Neumaier, T.; Steichele, E. *J. Phys. C: Solid State Phys.* **1982**, *15*, 4835−4846.
(7) Landers, J.; Salamon, S.; Escobar Castillo, M.; Lupascu, D. C.; Wende, H. *Nano Lett.* **2014**, *14*, 6061−6065.
(8) Mojir Shaibani, P.; Prashanthi, K.; Sohrabi, A.; Thundat, T. *J. Nanotechnol.* **2013**, *2013*, 1−6.
(9) Wang, L.; Han, Y.; Jia, G.; Zhang, C.; Liu, Y.; Liu, L.; Wang, C.; Cao, X.; Yin, K. *J. Nanosci. Nanotechnol.* **2011**, *11*, 5207−5209.
(10) Gao, F.; Chen, X.; Yin, K.; Dong, S.; Ren, Z.; Yuan, F.; Yu, T.; Zou, Z.; Liu, J.-M. *Adv. Mater.* **2007**, *19*, 2889−2892.
(11) Moniz, S. J.; Blackman, C. S.; Southern, P.; Weaver, P. M.; Tang, J.; Carmalt, C. J. *Nanoscale* **2015**, *7*, 16343−16353.
(12) Li, S.; Zhang, J.; Kibria, M. G.; Mi, Z.; Chaker, M.; Ma, D.; Nechache, R.; Rosei, F. *Chem. Commun.* **2013**, *49*, 5856−5858.
(13) Ederer, C.; Spaldin, N. A. *Phys. Rev. B: Condens. Matter Mater. Phys.* **2005**, *71*, 224103.
(14) Dho, J.; Qi, X.; Kim, H.; MacManus-Driscoll, J. L.; Blamire, M. G. *Adv. Mater.* **2006**, *18*, 1445−1448.
(15) Bernardo, M. S.; Jardiel, T.; Peiteado, M.; Caballero, A. C.; Villegas, M. *J. Eur. Ceram. Soc.* **2011**, *31*, 3047−3053.
(16) Xu, J.-H.; Ke, H.; Jia, D.-C.; Wang, W.; Zhou, Y. *J. Alloys Compd.* **2009**, *472*, 473−477.
(17) Prado-Gonjal, J.; Villafuerte-Castrejon, M. E.; Fuentes, L.; Moran, E. *Mater. Res. Bull.* **2009**, *44*, 1734−1737.
(18) (a) Wu, J.; Mao, S.; Ye, Z.-G.; Xie, Z.; Zheng, L. *J. Mater. Chem.* **2010**, *20*, 6512−6516. (b) Ortiz-Quiñonez, J. L.; Díaz, D.; Zumeta-Dubé, I.; Arriola-Santamaría, H.; Betancourt, I.; Santiago-Jacinto, P.; Nava-Etzana, N. *Inorg. Chem.* **2013**, *52*, 10306−10317.
(19) Song, J.-H.; Nam, J.-H.; Cho, J.-H.; Kim, B.-I.; Chun, M.-P. *J. Korean Phys. Soc.* **2011**, *59*, 2308−2312.
(20) Moniz, S. J. A.; Quesada-Cabrera, R.; Blackman, C. S.; Tang, J.; Southern, P.; Weaver, P. M.; Carmalt, C. J. *J. Mater. Chem. A* **2014**, *2*, 2922−2927.
(21) (a) Schiwon, R.; Metzinger, R.; Pfirrmann, C.; Limberg, C. Z. *Z. Naturforsch., B: J. Chem. Sci.* **2013**, *68*, 561−568. (b) Schiwon, R.; Schax, F.; Braun, B.; Limberg, C. *J. Organomet. Chem.* **2016**, DOI: 10.1016/j.jorganchem.2016.02.041.
(22) Pisarevskii, A. P.; Martynenko, L. I.; Dzyubenko, N. G. *Zh. Neorg. Khim.* **1990**, *35*, 1489−1493.
(23) Park, T. J.; Papaefthymiou, G. C.; Viescas, A. J.; Moodenbaugh, A. R.; Wong, S. S. *Nano Lett.* **2007**, *7*, 766−772.
(24) Shamir, N.; Gurewitz, E.; Shaked, H. *Acta Crystallogr., Sect. A: Cryst. Phys., Diffr., Theor. Gen. Crystallogr.* **1978**, *34*, 662−666.
(25) Singh, A. K.; Kaushik, S. D.; Kumar, B.; Mishra, P. K.; Venimadhav, A.; Siruguri, V.; Patnaik, S. *Appl. Phys. Lett.* **2008**, *92*, 132910.
(26) Landers, J.; Salamon, S.; Escobar Castillo, M.; Lupascu, D. C.; Wende, H. *Nano Lett.* **2014**, *14*, 6061−6065.
(27) Rusakov, V.; Pokatilov, V.; Sigov, A.; Matsnev, M.; Gubaidulina, T. *Mater. Sci. Eng., B* **2014**, *4*, 302−309.
(28) Sosnowska, I.; Peterlin-Neumaier, T.; Steichele, E. *J. Phys. C: Solid State Phys.* **1982**, *15*, 4835−4846.
(29) Escobar Castillo, M.; Shvartsman, V. V.; Gobeljic, D.; Gao, Y.; Landers, J.; Wende, H.; Lupascu, D. C. *Nanotechnology* **2013**, *24*, 355701.
(30) Kostiner, E.; Shoemaker, G. L. *J. Solid State Chem.* **1971**, *3*, 186−189.
(31) Park, T. J.; Papaefthymiou, G. C.; Moodenbaugh, A. R.; Mao, Y.; Wong, S. S. *J. Mater. Chem.* **2005**, *15*, 2099−2105.
(32) Ramirez, F. E. N.; Pasca, G. A. C.; Souza, J. A. *Phys. Lett. A* **2015**, *379*, 1549−1553.
(33) Giaquinta, D. M.; Papaefthymiou, G. C.; zur Loye, H.-C. *J. Solid State Chem.* **1995**, *114*, 199−205.
(34) Sheldrick, G. M. *SADABS*; University of Göttingen: Göttingen, Germany, 1996.
(35) Sheldrick, G. M. *SHELXS-97*; University of Göttingen: Göttingen, Germany, 2013.
(36) (a) Sheldrick, G. M. *SHELXL-2013*; University of Göttingen: Göttingen, Germany, 2013. (b) Sheldrick, G. M. *Acta Crystallogr., Sect. C: Struct. Chem.* **2015**, *71*, 3−8.
(37) https://www.uni-due.de/~hm236ap/hoersten/home.html.

DOI: 10.1021/acs.inorgchem.6b00951
Inorg. Chem. XXXX, XXX, XXX−XXX